Colloids and Surfaces A: Physicochemical and Engineering Aspects 617 (2021) 126386

Contents lists available at ScienceDirect

Colloids and Surfaces A: Physicochemical and Engineering Aspects

journal homepage: www.elsevier.com/locate/colsurfa

Synthesis, characterization and visible light-responsive photocatalysis properties of Ce doped CuO nanoparticles: A combined experimental and DFT+U study

Muhammad Rakibul Islam [a,*], Md. Saiduzzaman [a], Sadiq Shahriyar Nishat [b], Alamgir Kabir [b], S. F.U. Farhad [c]

[a] Department of Physics, Bangladesh University of Engineering and Technology (BUET), Dhaka, Bangladesh
[b] Department of Physics, University of Dhaka, Dhaka, Bangladesh
[c] Industrial Physics Division, Bangladesh Council of Scientific & Industrial Research (BCSIR), Dhaka, Bangladesh

GRAPHICAL ABSTRACT

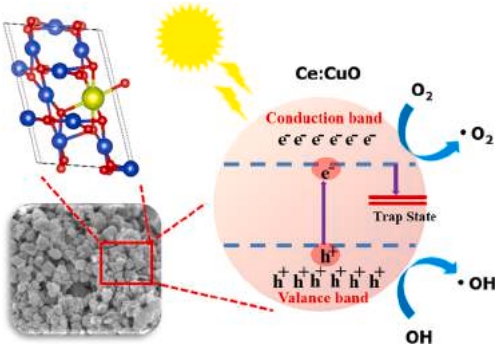

ARTICLE INFO

Keywords:
Nanoparticles
CuO
Ce-doping
Photocatalytic activity
DFT+U
Ab-initio

ABSTRACT

In this work, CuO and Ce doped CuO (Ce:CuO) nanoparticles (NPs) were prepared by the sol-gel auto-combustion process. The effect of the concentration of Ce doping (0, 2%, 4%, 6%, and 8%) on the structural properties, surface morphology, electronic properties, optical properties, and visible light assisted photocatalytic activities of NPs were studied experimentally and also with Density Functional Theory (DFT + U) simulation. The X-ray Diffraction (XRD), Raman and Fourier transform-infrared (FTIR) studies confirmed the presence of Cu-O bonding in the as-prepared nanoparticles. Incorporation of Ce was found to introduce intrinsic defects in the Ce:CuO NPs and reduces the optical bandgap from 1.72 eV to 1.40 eV. The photocatalytic performance of the NPs was assessed by studying the degradation of methylene blue (MB) under visible light irradiation. Ce:CuO NPs exhibit better photocatalytic efficiency compared to pure CuO NPs. Furthermore, DFT based simulation predicted that

* Corresponding author.
E-mail address: rakibul@phy.buet.ac.bd (M.R. Islam).

https://doi.org/10.1016/j.colsurfa.2021.126386
Received 20 December 2020; Received in revised form 8 February 2021; Accepted 24 February 2021
Available online 28 February 2021

the incorporation of Ce narrowed down the bandgap of the NPs due to the creation of shallow doping states near the valance and conduction bands. The reduction of band gap together with the presence of shallow dopant states allows efficient charge separation together with improved photon adsorption of Ce doped CuO NPs yielding an enhanced photocatalytic activity.

1. Introduction

The presence of different organic and inorganic pollutants in water due to industrial, agricultural, and domestic activities has led to a global need for the development of new, improved, and advanced technologies that can effectively improve water quality. In the past decades, photocatalysis has gained tremendous attention both from industrial and research point of view and is considered a promising technique for wastewater treatment as it offers an easy, economic, and sustainable route for the decontamination of water [1,2]. Photocatalysis is a process in which photon-induced electron-hole pairs are generated in a photocatalyst which performs oxidation and removes toxic elements from the adjacent water molecule [3]. Photosensitivity, high oxidizing power, nontoxicity, and easy availability has made TiO_2 and ZnO as popular choices for photocatalysis [4–7]. However, due to their large optical bandgap (E_g), TiO_2 and ZnO require illumination of high energy ultraviolet (UV) light to establish photodegradation. This limits the applicability of these materials since the production of UV light is costly. Moreover, the spectral distribution of solar energy contains ~45 % visible light as compared to ~5% of UV light, widespread applications of photocatalysis is therefore possible if the catalysis procedure can be performed under easily available cost-efficient visible light.

Copper oxides are abundant in nature and thus inexpensive as well as the most widely used bio-compatible materials which play an imperative role in different biological and technological applications including antibacterial activity, adsorbent, gas sensor [8–12], optoelectronic devices (for example, thin-film transistors and solar cell [13], etc. Out of various copper oxide phases, the two most stable phases are cubic cuprous oxide (Cu_2O) and monoclinic cupric oxide (CuO), possess bandgaps ~ 1.4 eV–2.17 eV with useful semiconducting properties [13,14]. They can be considered as a potential alternative of wide bandgap (Eg = 3.1–3.4 eV) TiO_2 and ZnO for visible light photocatalysis [15,16]. In the case of photocatalytic applications, CuO preferred over Cu_2O due to its superior stability and lower bandgap [13] which enable its optical bandgap to tune by suitable metal doping for utilizing a wide range of visible (solar/synthetic) radiations. The extreme reactivity of copper (Cu^{2+}) together with the low bandgap of CuO makes it a promising photocatalyst for the decontamination of water [17]. For phase pure CuO, the electrons in the conductions band are unstable, most of the photo-generated electrons move to the valance band and recombine with the hole without taking part in the oxidation process [18]. The efficiency of photocatalysis can, therefore, be improved by retarding the charge carrier recombination process.

Different techniques, namely surface modification, transition, and rare earth metal doping, etc. were employed to slow down the photogenerated electron-hole recombination in CuO [19–24]. Among them, doping of rare earth elements in CuO is considered one of the most effective ways as it can retard the recombination rate by introducing localized impurity/defect states near the VBM or CBM (or both) that can trap the light-generated electrons and enhance the photocatalytic performance [21]. Furthermore, rare-earth elements are found to reduce the bandgap CuO, which allows faster transition of charge carriers through the forbidden gap, thereby, reduces the charge-carrier recombination [21–24]. Additionally, rare earth elements can enhance the photogenerated electron-hole production due to their improved photoresponse.

Various rear earth metals, including La, Pr, Sm, Tb, Ce etc. were used to enhance the photocatalytic performance of CuO [20–22]. Among them, Ce is considered as a popular dopant metal for CuO because of its biocompatibility and non-toxicity. Ekthammathat et al. have prepared Ce doped CuO nano-leaves using the co-precipitation method and showed enhanced photocatalytic performance of CuO under UV light illumination. Chen et al. have prepared CuO nanostructure by hydrothermal technique22]. They showed that Ce doping tune the bandgap of the nanoparticles and improve the UV assisted photocatalytic activity of the nanostructure [25]. In another report, Chaudhari et al. showed that Ce doped CuO was prepared by the sonochemical method that demonstrates 98 % dye degradation induced by solar-irradiation [26]. Even though several types of research were performed to evaluate the photocatalytic activity of Ce doped CuO, which demonstrates improved photocatalytic performance under UV light illumination. However, considering its promising potential in pollutant decontamination, visible-light-driven photodegradation is necessary for the economic viability and sustainability. Nonetheless, the detailed study on the visible light assisted photocatalytic performance of Ce:CuO is still inadequate. Consequently, the major objective of this article is to study the effect of Ce dopant on the structural, morphological, electronic, and optical properties together with the visible light assisted photocatalytic efficiency of CuO nanoparticles.

A deep understanding of the photocatalysis mechanism of Ce:CuO photocatalyst is necessary for the large-scale application of the photocatalysts for environmental cleaning applications. A number of research article has been published on the photocatalysis of Ce:CuO describing the effect Ce content on the photodegradation efficiency based on experimental findings [22,27,28]. A theoretical analysis on the other hand may helps realizing the interaction between dopant with the host molecule and the corresponding change in band structure of the photocatalyst which is nacessary to understand the photocatalysis mechanism [29–31]. A combined experimental and theoretical investigation is, therefore, indipensable to comprehend the role of Ce dopant on the photocatalytic performance of CuO NPs. However, to the best of our knowledge, there exist no reports on the experimental finding of the influence of concentration of Ce on the photocatalytic performance of CuO nanoparticles corroborated by the theoretical analysis. That is why density functional theory (DFT) was used to carry out the theoretical investigation. DFT is the highest-level quantum mechanics based theory to investigate various types of properties of a system. It is a widely accepted method used in different fields like condensed matter, material science, chemistry, etc. Due to this wide acceptance of using this simulation method, we used this simulation method to investigate our desired properties of the system.

The nanoparticle preparation techniques play an important role in controlling their properties. Several techniques are used for the preparation of CuO NPs, which include the sol-gel process [32], solid-state reaction [33], co-precipitation [22], sono-chemical method [26], hydrothermal techniques [25], microwave irradiation [28], and thermal decomposition method [34], etc. Among them, the sol-gel auto--combustion technique offers a versatile, rapid, easy, and economic route for the preparation of NPs that includes a self-sustained reaction in a solution of different oxidizers and fuels [35–37].

In the present work, pure and Ce doped CuO nanoparticles ware synthesized by a facile sol gel auto combustion technique. The structural and optical properties of the as-prepared nanoparticles were analyzed by FTIR, XRD, FE-SEM, Raman and UV–vis spectroscopy. Besides, the effect of the contents Ce on the photocatalytic performance of the NPs was also evaluated experimentally. The results show that incorporation of Ce reduces the optical band gap and thereby improve the photocatalytic performance of the CuO NPs. Furthermore, a DFT + U based theoretical

investigation was performed to shed light on the possible interaction and charge transitions between Ce and CuO which yielded result which is consistent with the experimental conclusion. The synergy between the experimental and computational techniques allows us to offer a complete picture about the influence of Ce on the phodegradation of CuO nanoparticles by providing a possible mechanism at an atomistic level.

2. Material and methods

2.1. Chemicals

CuO NPs were synthesized via a sol-gel auto-combustion technique similar to work by Islam et al. [38]. Briefly, Copper nitrate ($Cu(NO_3)_2.3H_2O$), Cerium Nitrate ($Ce(NO_3)_4.6H_2O$) served as the precursors for Cu and Ce respectively. The citric acid ($C_6H_8O_7$) and Deionized (DI) water (~18 MΩ.cm) were chosen as fuel and solvent respectively. A 1:1 ratio between The fuel and oxygen was maintained during the synthesis of NPs.

2.2. Synthesis procedure

Aqueous solution of 0.1 M copper nitrate and 0.1 M citric acid were made separately followed by stirring at ambient for one hour. Once dissolved, the stock solution is produced by mixing the two solutions into a glass beaker followed by stirring at 50 °C. The solution pH was made neutral by adding an appropriate amount of NH_3 solution. Then the solution temperature was raised gradually at a constant rate yielding the gel at 74 °C. At ~ 90 °C, the gel starts burning as the combustion process began. The CuO nanoparticles were then amassed from the ashes. For the synthesis of Ce:CuO nanoparticles cerium nitrate solution of various concentrations (0%, 2%, 4%, 6%, and 8%) wax mixed with the citric acid and copper nitrate solution. Hence the formulation process similar to that of the CuO nanoparticle preparation process was followed.

2.3. Characterization

Following the preparation of the nanparticle, their physical properties, and photocatalytic performance were studied. The different structural parameters of the NPs such as lattice parameters, bond angles, bond lengths, micro stress and strain, crystalline size were determined from the X-ray diffraction (XRD) technique. XRD was carried out using an X-ray diffractometer (3040XPert PRO, Philips) using CuK_α radiation having wavelength 1.5406 Å. The surface morphology of the nanoparticles was studied by Field emission scanning electron microscopy (FE-SEM) (JSM 7600, Jeol). The chemical analysis was performed by Fourier transform infrared spectroscopy (FTIR) in attenuated total reflection (ATR) mode using a (Shimadzu IRSpirit) spectrophotometer at a spectrum range of 400-4000 cm^{-1}. Raman analysis was carried out at room temperature using 785 nm diode laser (Power $\leq$ 5 mW) as an excitation source (HORIVA MacroRam) to study the vibrational structure of the synthesized NPs. The band gap of the nanoparticles was calculated from diffuse reflectance data collected by a UV–vis-NIR spectrophotometer (Shimadzu ISR 2600plus) with a custom-made powder sample holder. Standard $BaSO_4$ powder (Shimadzu P/N#200−53627) was used for baseline corrections before the actual measurements.

2.4. Photocatalytic activity measurement

The photocatalytic activity of CuO and Ce:CuO NPs was assessed by studying the decolorization of methylene blue (MB) solution under visible light illumination similar to our previous study [37]. At first, 20 mg of the photocatalyst was mixed into 40 mL of 10-mg/L aqueous solution of MB. To attain stable adsorption of MB molecules, the solution was kept in dark for 1 h followed by magnetic stirring. The solution was then placed into the photocatalytic chamber and was illuminated by a 24 W LED light for a particular duration of time and the irradiated solution collected. After that, the photocatalyst NPs were precipitated from the suspension by a centrifuge machine. The absorption spectra of the supernatants were monitored by the UV–vis spectrometer in photometric mode.

2.5. Computational methods

Systematic studies on the structural, electronic, and optical properties of the pure and Ce doped CuO were carried out using DFT approximation as implemented in the VASP simulation package [39,40]. One of the limitations of DFT approximation is that these approximations cannot estimate the exact experimental bandgap for the materials having strong electronic correlation, it severely underestimates the bandgap of strongly correlated materials. Since CuO is a strongly correlated material, in this analysis, we are using the Hubbard DFT + U correction scheme, originally introduced in Refs. [41]. The DFT + U approach is widely used for the study of several transition-metal compounds [42,43]. There are more accurate computation methods available like hybrid functional (HSE06) [44], GW functional [45], but these are computationally very expensive. However, It is found in the literature that the hybrid functional (HSE06) gave overestimated bandgap of 2.74 eV compared to experimental results [46].

The unit cell of CuO contains four Cu and four O atoms and it has space group C 2/c. However, we have used the supercell approach to simulate doped systems [38,47,48]. Generalized gradient approximation (GGA) [49] is used as pseudo potential and for the exchange-correlation functional we have used Perdew-Burke-Ernzerhof (PBE) [49]. The 3d, 4 s, and 4p electrons of Cu, and 2 s and 2p electrons of O are considered as valance electrons in this study. For the relaxation of the unit cell, sampling density of $11 \times 11 \times 6$ k-points with Monkhorst-Pack [50] scheme, and 520 eV was used as plane wave cut-off energy. The maximum values of displacement 0.015 Å, energy change 1×10^{-8} eV·atom-1, max force 0.01 eV $Å^{-1}$ were set as the convergence tolerances for geometry optimization calculations. For the density of state (DOS) calculation a denser k-point mesh of $17 \times 17 \times 10$ and tetrahedron smearing method was used. The spin-polarized scheme of DFT with anti-ferromagnetic ordering is used for all the calculations. The Hubbard potential of U_{eff} =7.14 eV [51–53] and U_{eff} =4.5 eV [54,55], was added to the strongly localized 3d orbitals of Cu and 4f orbitals of Ce respectively. For understanding the effect of Ce doping in CuO having different concentrations 4 different supercells ($3 \times 2x1$, $2 \times 2x2$, $3 \times 2 \times 2$, and $4 \times 3 \times 2$) have been modeled from CuO unit cell. One of the Cu atoms has been replaced by one Ce atom from the $3 \times 2x1$, $2 \times 2x2$, $3 \times 2 \times 2$, and $4 \times 3 \times 2$ CuO supercells to obtain 8.33 %, 6.25 %, 4.17 %, and 2.08 % Ce concentration respectively. These concentrations have been used to compare the results with our experimental concentrations of Ce which are 8%, 6%, 4%, and 2%. The supercells are shown in Fig. 1.

To understand the optical behavior, the independent particle approximation (IPA) method was used. We did not take into account the quasiparticle self-energy corrections, the local-field corrections, and the excitonic effects. We integrated the occupied and reasonable number of unoccupied bands to calculate the imaginary part of the dielectric function. Then using Kramers–Kronig relations the real part of the dielectric function was calculated. Using these dielectric functions, we calculated the absorption coefficient and other optical properties.

3. Results and discussion

3.1. XRD analysis of CuO and Ce:CuO nanoparticles

The phase composition and crystalline structure of the CuO and Ce:CuO NPs were analyzed from the XRD pattern of respective NPs. The XRD data of the NPs were further investigated by the Rietveld

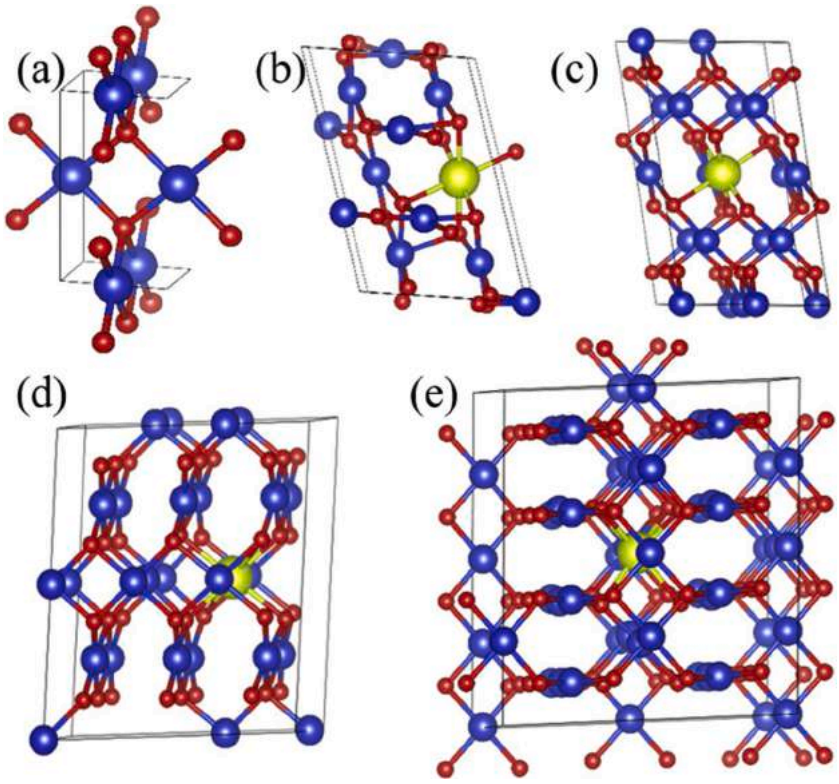

Fig. 1. Relaxed supercells for (a) 8.33 %, (b) 6.25 %, (c) 4.17 %, and (d) 2.08 % Ce doped CuO, and (e) the unit cell of pure CuO. Cu atoms are blue, O atoms are red and Ce atoms are yellow.

refinement technique. Rietveld refinement was performed using a FULLPROF package [56]. Rietveld refinement of the XRD pattern for the CuO and Ce:CuO NPs were presented in Fig. 2. The refined XRD patterns for different concentration of Ce doped NPs in the form of observed and calculated differences (Fig. 2) illustrate a good agreement between the observed and the calculated profiles.

Fig. 3a shows the variation of the XRD pattern for CuO and Ce:CuO NPs. The diffraction peaks correspond to the crystal planes (110), (-111), (111), (-202), (020), (202), (-113), (-311) and (220) observed at the 2θ value = 32.64°, 35.52°, 38.85°, 48.80°, 53.44°, 58.24°, 6157°, 66.24°, and 67.92° respectively, which confirms the monoclinic crystalline planes of CuO NPs [57]. No diffraction peaks from other copper oxide phases are discernible. The observed XRD pattern also matches with the standard JCPDS Card no. 05 0661 of phase pure CuO.

The sharp and highly intense diffraction peaks in the XRD profile indicate that the CuO NPs are highly crystalline. From the figure, it is found that the height of diffraction peaks reduces with the increase of Ce concentration suggesting a deterioration of the crystalline structure due to doping. Additionally, in contrast with the undoped CuO a new peak located at 2θ = 28.5° appears to increase with increasing Ce-doing which can be assigned to the (111) diffraction plane of cubic CeO_2 ; indexed with standard JCPDS Card No. 34-0394 [58]. A similar appearance of a new peak due to Ce doping was also observed in the reported literature [59–61]. The XRD results demonstrate that the synthesized Ce:CuO NPs are in a mixed phase of monoclinic CuO structure and of cubic CeO_2 structure [62]. A small shift in XRD peaks was also observed with the increase of Ce concentration. Such a shift may occur due to the difference in the atomic radius between Ce^{4+} (84 pm) and substituted Cu^{2+} (73 pm) [27]. A shift in diffraction peak, therefore, indicates the incorporation of Ce ions into the CuO lattice due to doping [62.

Rietveld analysis was also performed to obtain the FWHM, D-spacing, peak position, peak center, the relative intensity of the NPs from the XRD data. From the XRD data, the (-111) peak was found to be the dominant one and was used to extract the structural parameters of the NPs. The crystallite size of the NPs was calculated by the Scherer equation [63] :

$$D = 0.9\lambda/(\beta \cos\theta)$$

Where, λ is the X-ray wavelength (= 1.5406 Å). β and θ are the full width at half maximum (FWHM), and Bragg angle of the diffraction peak. Fig. 3b demonstrates the crystallite sizes of CuO and Ce:CuO nanoparticles and it was found to be reduced with the amount of Ce dopant. The reduction in the crystallite size of the NPs can be attributed to the delaying of the growth of CuO crystal due to the formation of Ce–O–Cu bond by Ce doping. Similar dopant-induced changes in the crystallite size of the NPs were observed in Ce-doped ZnO [59,61,64]. The lattice micro-strain of the NPs was also obtained from the Reitveld analysis and was found to increase with the amount of Ce dopant (Fig. 3b).

3.2. Raman spectroscopy of CuO and Ce:CuO nanoparticles

Room temperature Raman spectroscopy was carried out to further confirm the phase purity of CuO and to study the influence of Ce dopant on the vibrational structure of CuO NPs. Since the lattice vibration is very sensitive to chemical bonding nature, bond length, crystal structure, and variation of atomic masses [13,14], therefore, Raman spectra should confirm the single-phase CuO NPs as well as Ce-doping on its vibration structure. Fig. 4 demonstrates the Raman spectra of the as-synthesized pure and Ce-doped NPs. In the figure, three peaks are observed at 295 cm^{-1}, 343 cm^{-1} and 639 cm^{-1} corresponds to the A_g, B_{g1}, and B_{g2} mode of the CuO crystal [13,14,65]. No peaks corresponding to the Cu_2O vibrational modes are observed[14] in the Raman spectrum which confirms the presence of single-phase in the CuO NPs. For Ce:CuO NPs an additional peak is observed near 453 cm^{-1} which attributes to the Raman active mode of fluorite cubic CeO_2 which also confirms Ce doping in CuO NPs [62,66]. The observed Raman spectra

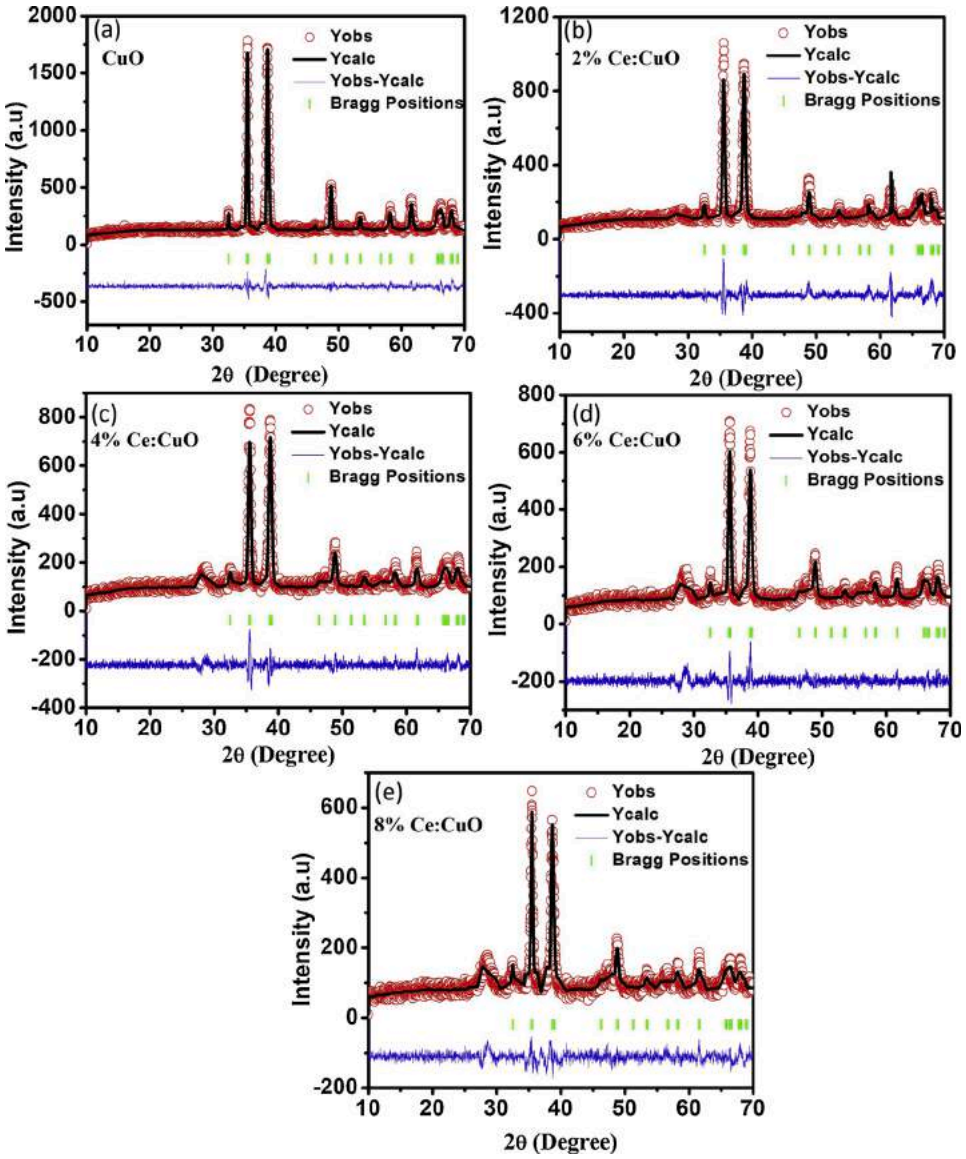

Fig. 2. Rietveld refined XRD patterns of Ce doped CuO nanoparticle for (a) 0% (b) 2.0 %, (c) 4.0 %, (d) 6.0 % and (e) 8.0 % Ce-dopant. Here the red circles correspond to the observed data (Yobs), the calculated patterns (Ycal) are represented by the black lines and their differences (Yobs-Ycal) are indicated by the blue bottom curves. The green bars correspond to Bragg positions of different planes of the corresponding samples.

show a reduction in peak height and a broadening in the FWHM of the peaks Ce doping. Since the width of the Raman line varies inversely with the mean free path, and therefore broadening in FWHM signifies the reduction of the mean free path. Fruthermore the broadening of the Raman bands may originates from the reduction of phonon lifetime due to scattering [67]. In the present case scattering results from the presence of defects introduced by Ce doping.

3.3. FTIR analysis of CuO and Ce:CuO nanoparticles

FTIR of the synthesized NPs was also conducted (recorded at room temperature in the range of 400 – 4000 cm^{-1}) to further confirm the phase purity of copper oxide as well as the effect of Ce-doping on its phonon modes. FTIR generally provides complementary information of phonon modes compared to Raman spectroscopy where symmetric vibrations are Raman active and asymmetric vibrations are IR active. Fig. 5 shows the FTIR spectra of the CuO and Ce:CuO NPs which exhibited several distinct absorption bands between 400 cm^{-1} – 1250 cm^{-1}.

The peaks at 1101 cm^{-1}, 1627 cm^{-1}, and 1658 cm^{-1} correspond to the stretching vibration of the carbonyl group of citric acid. Stretching vibrations of C═C bonds and C═O bond occur in 1101 cm^{-1} and 1658 cm^{-1} respectively. The peak at 1627 cm^{-1} represents the molecular H_2O (H—OH—) bending frequency. The peak located at 2373 cm^{-1} occurs due to atmospheric CO_2 present in the instrument [68]. Bands at 2926 cm^{-1} and 2860 cm^{-1} indicate to C—H stretching vibrations [28, 69]. A wideband with a peak at 3452 cm^{-1} occurs between 3600 cm^{-1} to 3100 cm^{-1} suggesting the presence of O—H stretching vibrations of the alcoholic and phenolic hydroxyl groups [69].

The peaks observed around at 426 cm^{-1}, 487 cm^{-1}, 530 cm^{-1}, 588 cm^{-1}, and 688 cm^{-1} correspond to the characteristic stretching vibrations of metal-oxygen (Cu-O) bond in the monoclinic CuO [28,70]. The absorption bands at 688 cm^{-1} and 588 cm^{-1} correspond to the Cu-O stretching along [-1 0 1] direction and that of 487 cm^{-1} corresponds to the Cu-O stretching along [1 0 1] direction. In the FTIR spectrum, no IR active vibrations for Cu_2O or impurities were observed, thus, confirming the formation of single-phase CuO in the nanoparticles. The absorption peak near 1230 cm^{-1} has been attributed to the starching vibration of

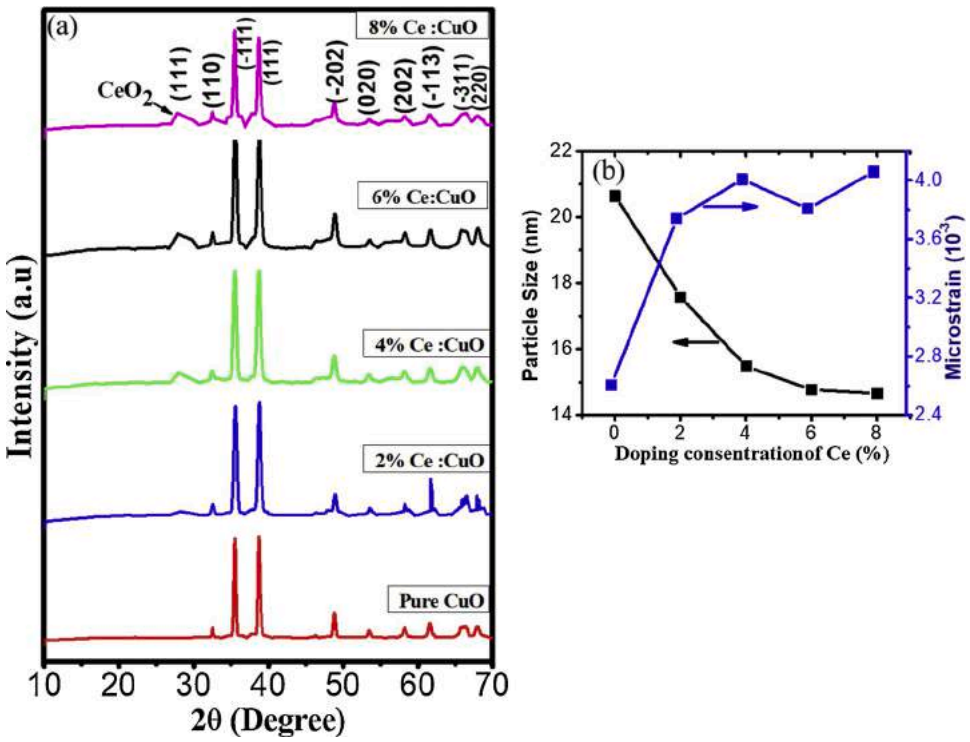

Fig. 3. (a) X-ray diffraction pattern of pure and Ce doped CuO nanoparticles (b) variation of particle size and microstrain as a function of Ce-dopant concentration in CuO nanoparticles.

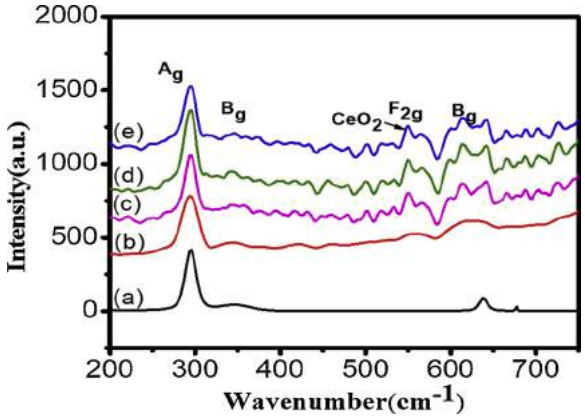

Fig. 4. Raman spectra of Ce doped CuO nanoparticle for (a) 0% (b) 2.0 %, (c) 4.0 %, (d) 6.0 % and (e) 8.0 % Ce-dopant. (Use the updated figure from MS power point slides).

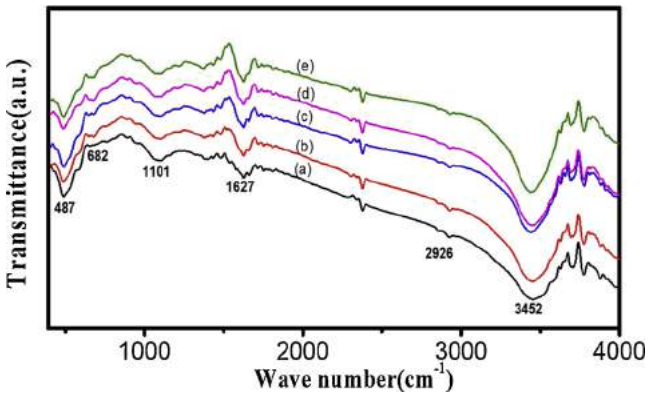

Fig. 5. Typical FTIR spectrum of Ce doped CuO nanoparticle for (a) 0% (b) 2.0 %, (c) 4.0 %, (d) 6.0 % and (e) 8.0 % Ce-dopant. (Use this in supporting materials and give only 400 – 1250 cm^{-1} range one from MS power point slides.).

the O–Cu = O and found to be decreasing with increasing Ce content [28], presumably due to the addition of Ce into the CuO lattice evident from the XRD results.

3.4. Surface morphology of CuO and Ce:CuO nanoparticles

Fig. 6 shows the FE-SEM micrographs of CuO and Ce:CuO NPs. Pure CuO NPs exhibit nanostructured particles with diameters range between 30−50 nm. Incorporation of Ce was found to reduce the particle size of CuO, and concentration and for 8% Ce:CuO NPs the particle size varies between 15−20 nm. Furthermore, the uniformity of the particle size distribution increases with the increase of Ce concentration. The observed lessening of the particle size of NPs due to Ce doping matches with the results obtained from the XRD analysis. Such a reduction in particle size may be ascribed to the inhibition of particle growth after nucleation due to rear earth Ce doping.

3.5. Optical properties of CuO and Ce:CuO nanoparticles

Diffuse reflectance spectroscopy was used to estimate the bandgap of the nanoparticles. The Kubelka-Munk function *F(R)* yield a relationship between the reflectance (*R*) and the absorption coefficient (α): [38]:

$$F(R) = (1\text{-}R)^2/2R = \alpha/s$$

where *R* is the reflectance and *s* is scattering co-efficient and α is the absorption coefficient. The Tauc equation set a relationship between the band gap (E_g) and absorption coefficient (α), and is given by [38]:

$$\alpha h\nu = A(h\nu - E_g)^n$$

Where *A* is a proportionality constant, $h\nu$ is the energy of incident light. The exponent $n = 1/2$ for the direct allowed optical transition. By

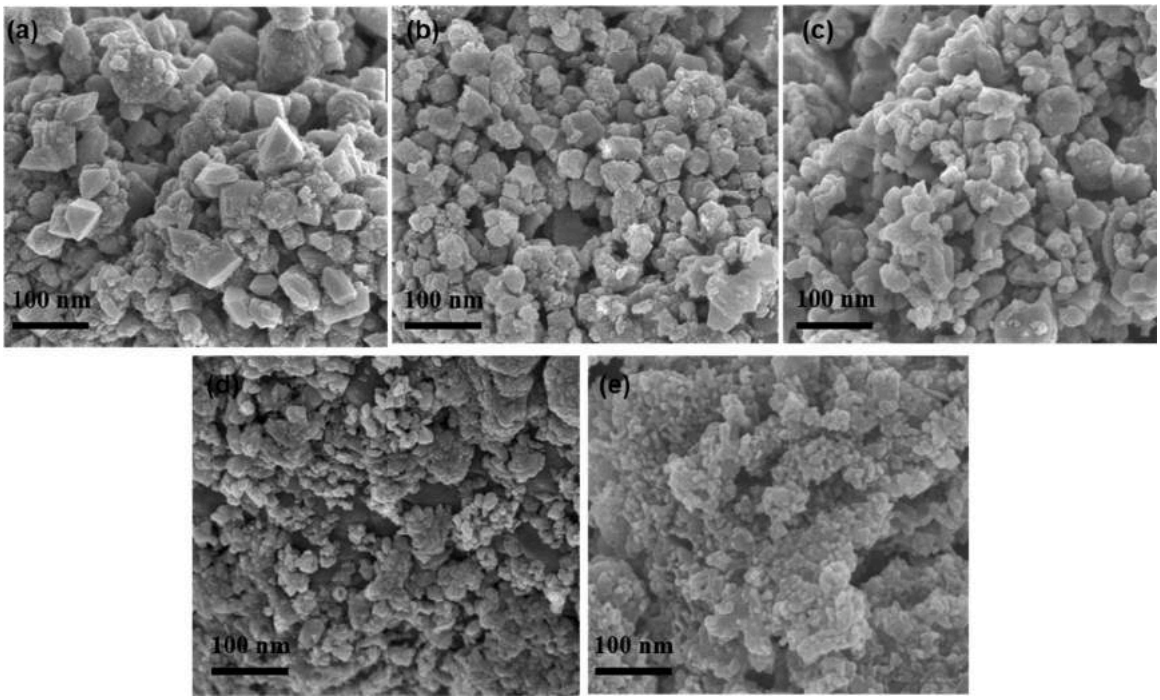

Fig. 6. SEM micrograph of synthesized Ce doped CuO nanparticles for (a) 0% (b) 2.0 %, (c) 4.0 %, (d) 6.0 % and (e) 8.0 % Ce-dopant.

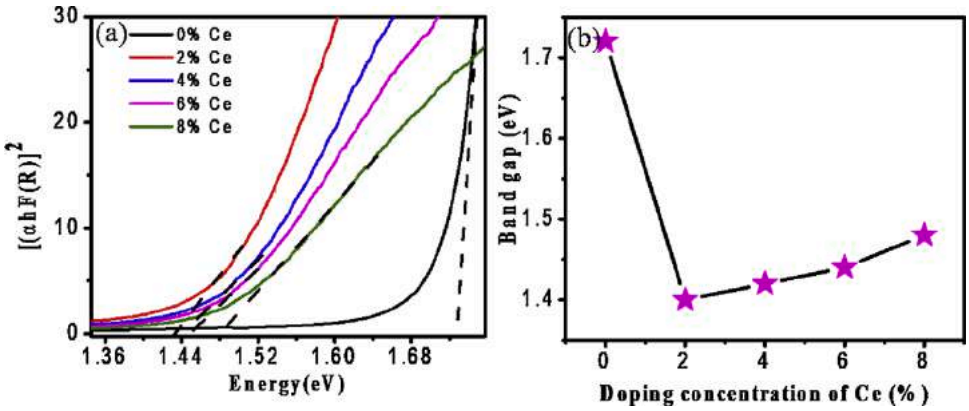

Fig. 7. (a) Tauc plot of the Kubelka-Munk function for estimating the band gap of pure CuO and Ce-doped CuO nanoparticles (b) variation of optical band gap as a function doping concentration of Ce in CuO nanoparticles.

considering the coefficient s as a constant we can say that the *F(R)* is proportional to α. Then the Tauc relation can be rewritten in terms of Kubelka-Munk function: $(h\nu F(R))^2 = (A/s)(h\nu - E_g)$.

The band gap of the NPs can be obtained by extrapolating the straight-line portions of the curves the $(h\nu F(R))^2$ *vs* $h\nu$ plot (Fig. 7). Fig. 7a shows the extraction of the E_g values for CuO and Ce:CuO NPs from the plot of $(h\nu F(R))^2$ *vs* $h\nu$ curve. The optical band gap was found to be 1.74 eV for pure CuO [38] which matches the reported value [71,72]. Fig. 7b shows the variation of band gap of the NPs with Ce concentration. Ce doping was found to diminish the band gap of the NPs. Such a reduction in band gap can be ascribed to the presence of impurity states in between the conduction and valance band of the CuO originating from the Ce doping [73,74]. With the increase of the number of dopant atoms these impurity states combine to the lowermost edges of the conduction band and thereby reduces the gap between the conduction and valance band [74,75].

From Fig. 7b it was also observed that when the Ce doping concentration is more than 2%, the band gap increases at a slow rate with dopant concentration and reaches 1.5 eV for 8% Ce doping. Such an increase in band gap may be attributed to the Burnstein-Moss (BM) effect [76]. When the semiconductor is heavily doped then the Fermi level can move towards the conduction band and as a consequence, the valance band electron requires more energy to move to the unoccupied state of the conduction band resulting in an increase of band gap [77].

3.6. Photocatalytic activity of CuO and Ce:CuO nanoparticles

The photocatalytic activity of CuO and Ce:CuO NPs were estimated by studying the absorbance spectra of MB solution irradiated by visible light and is presented in Fig. 8. The intensity of the absorption spectra was found to be reduced with the period of light illumination for both CuO and Ce:CuO catalysts. To assess the photocatalytic performance, the reduction of the height of the absorbance peak at ~664 nm with time was monitored.

Fig. 9a shows the photocatalytic degradation rate of MB solutions with CuO, and Ce:CuO NPs. It is evident that Ce doping increases the photocatalytic degradation rate of the NPs. 2% Ce doping yields the highest degradation rate and the degradation rate reduces with the

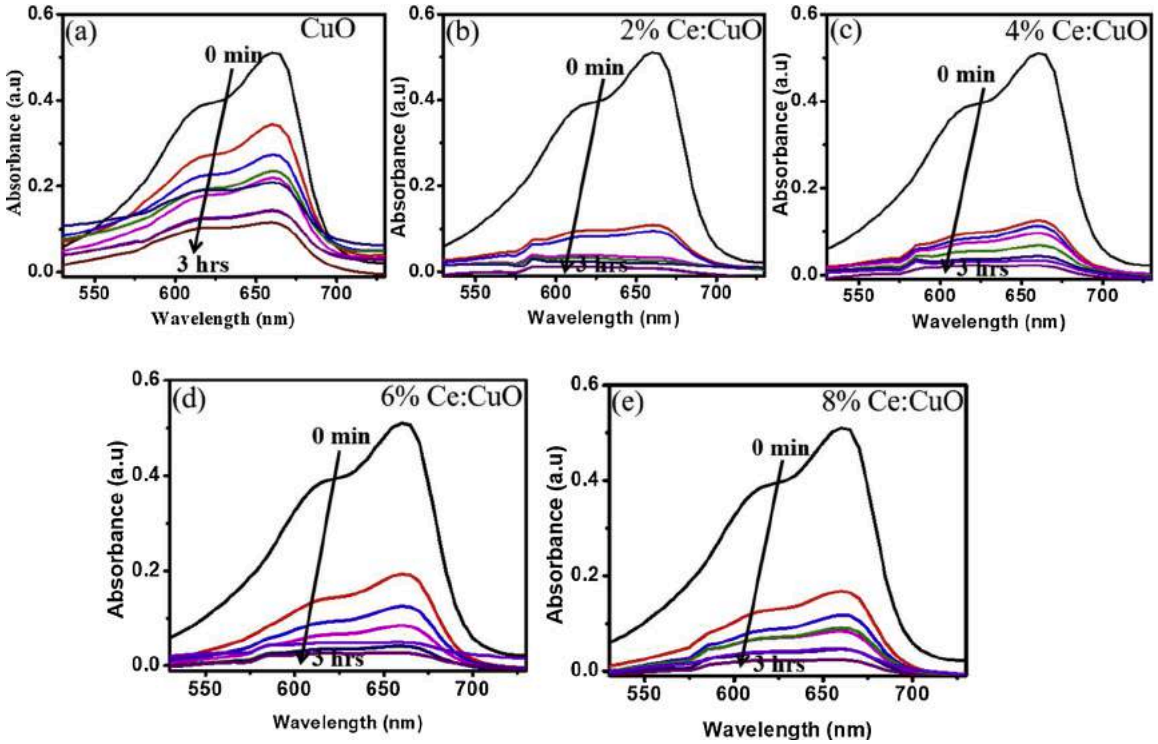

Fig. 8. The variation in UV–vis absorption spectra of methylene blue (MB) dye solution as a function of irradiation time in the presence of (a) pure CuO and (b) 2% Ce:CuO, (c) 4% Ce:CuO (d) 6% Ce:CuO and (e) 8% Ce:CuO nanoparticles as a catalyst under visible light illumination.

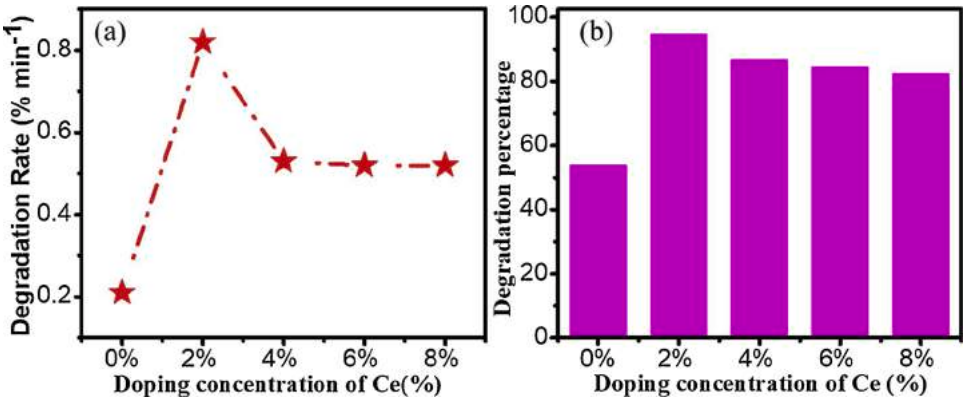

Fig. 9. Plots of (a) degradation rate and (b) degradation percentage MB dye as function doping concentration of Ce in CuO nanoparticles.

increase of Ce concentration. Fig. 9b shows the variation of degradation percentage of the MB dye due to CuO and Ce:CuO NPs after 30 min of photon illumination. It shows that undoped CuO can degrade 60 % of the dye after 30 min of irradiation. Whereas for 2% Ce doped NPs show almost complete photo-degradation (99 %) of the MB dye for the same duration. The degradation percentage reduces slightly for the concentration of Ce dopant greater than 2%. However, in all cases, the degradation percentage of Ce:CuO NPs are greater than that of pure CuO NPs.

(Fig. 10) represents a schematic diagram that depicts the photocatalysis reaction mechanism of CuO and Ce:CuO NPs. During visible light illumination, electrons from the valance band move to the conduction band and electron/hole (e^-/ h^+) pairs are formed. The hole produced hydroxyl radicals ($^{\bullet}OH$) by oxidizing the water molecule near the surface. The electron reacts with the oxygen molecules and produces superoxide radicals ($^{\bullet}O_2^-$). The radicals oxidized and degrade the MB dye present in the aqueous solution. The corresponding reaction mechanism is given below [78]

$$CuO + h\nu \rightarrow e^- + h^+$$

$$H_2O + h^+ \rightarrow OH^- + H^+$$

$$e^- + O_2 \rightarrow {}^{\bullet}O_2^-$$

$${}^{\bullet}O_2^- + H^+ \rightarrow HO_2$$

$$HO_2 + {}^{\bullet}O_2^- + H^+ \rightarrow H_2O_2 + O_2$$

$$H_2O_2 + e^- \rightarrow OH^- + {}^{\bullet}OH$$

$${}^{\bullet}O_2^- + OH\text{-} + \text{dye} \rightarrow \text{Degrade Pollutant}$$

The improvement of the photocatalytic performance of CuO NPs due to Ce doping can be attributed to several reasons. In CuO NPs, the photocatalytic efficiency reduces due to electron-hole recombination. Ce doping can improve the photocatalytic efficiency by enhancing the mean lifetime of electron and thereby retarding the charge carrier recombination [78]. For Ce:CuO NPs, the Ce^{4+} ions trap the photo-generated electrons and as a result, they cannot move to the valance

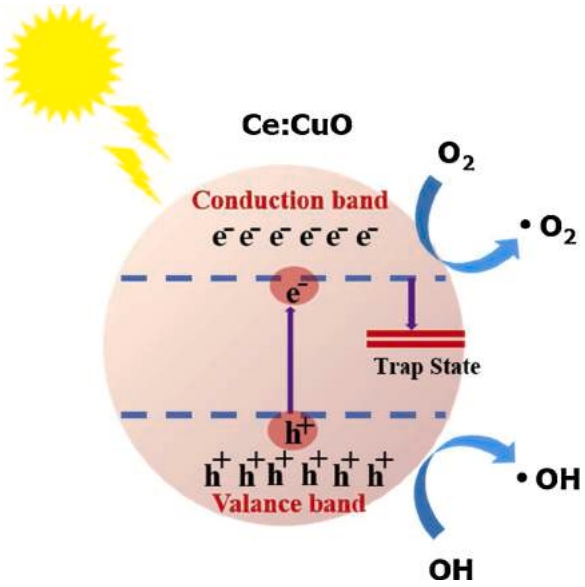

Fig. 10. Schematic diagrams showing the photo-catalytic mechanism of Ce doped CuO nanoparticles.

band resulting in a reduction in electron-hole recombination rate [79].

The surface area of the nanostructured particles plays a significant role during photocatalysis as the photo-generated charge carriers move to the surface and the oxidization process occurs there [80]. From the structural properties and surface morphology of the NPs, it was confirmed that Ce doping reduces the particle size of the NPs. Since the lowering of particle size increases the surface area of NPs, more dye molecules can come close to the surface of the catalyst and thereby improve the efficiency of photocatalysis [81]. Furthermore, the optical properties demonstrate that Ce doping reduces the band gap of CuO. Therefore the Ce:CuO NPs require less energy to produce electron-hole pairs at low energy, causing utilization of more photons to take part in photocatalysis resulting in an increased photocatalytic efficiency [38, 82,83].

Fig. 9 shows that 2% Ce doping provides excellent photocatalytic efficiency and the photocatalytic performance slows down for 4%, 6%, and 8% Ce-doping. The photocatalytic efficiency (Fig. 10) and the optical band gap (Fig. 8b) of Ce:CuO NPs follow the same trend. Fig. 8b shows that 2% Ce doped CuO NPs has the lowest band gap. As a result, more charge carriers can take part in photocatalysis for 2% Ce:CuO NPs than other NPs with higher Ce concentration. Thus the improved photocatalytic performance of Ce:CuO NPs can be accredited to a synergistic effect between band gap narrowing and particle size reduction of the NPs that occurred by Ce doping.

3.7. DFT analysis

3.7.1. Structural and electronic properties

The dopants and the host atoms in the lattice have different atomic radii, so the crystal structure will change after the doping. In Table 1, the average bond lengths are presented. There is a large change of bond length near the position of the dopant, this is due to the electronegativity difference between the host and the dopant atoms. A distortion of the crystal structure is revealed from the relaxed structure. As concentration increased, the Ce-O bond length decreased gradually. As Ce atoms become more closely spaced for higher concentration i.e. for smaller supercell, stronger impurity-impurity interaction reduced the bond length between Ce and O.

Table 1
Bond lengths of Cu-O and Ce-O for pure and different concentrations of Ce doped CuO obtained from the theoretical study.

Element	Bond length (Cu-O) near Ce atom	Bond length (Ce-O)
Pure CuO	1.94 Å(GGA), 1.927 (GGA + U)	N/A
2% Ce doped CuO	1.96 Å (GGA + U)	2.446 Å (GGA + U)
4% Ce doped CuO	1.96 Å (GGA + U)	2.424 Å (GGA + U)
6% Ce doped CuO	2.02 Å (GGA + U)	2.305 Å (GGA + U)
8% Ce doped CuO	2.01 Å (GGA + U)	2.282 Å (GGA + U)

The CuO structure is formed by the square planer orientation of the Cu and O atoms. After replacing the Cu atom with Ce, the Ce atom took the octahedral orientation with the O atoms. But this octahedral orientation is moderately distorted and reduces the symmetry of the system. The centers of the positive and the negative charges can get separated due to this lack of symmetry and distortion in the systems. This type of doping effect can produce some local internal electric field in the lattice, which can result in octahedral dipole moments. The photocatalytic activity would greatly enhance the doped CuO by reducing the recombination process of photo-generated electron-hole pairs. Thus, degradation rates can be increased. Moreover, due to this distortion and lack of symmetry, particle size decreases as increasing the concentration found in our experiment (see Figs. 3 and 6).

As we know that the standard DFT underestimates the bandgap of a strongly correlated system such as CuO, we have used the DFT + U formalism. The value of U_{eff} =7.14 eV was used for the 3d orbital of Cu that gave a bandgap of 1.74 eV which also matches our experimentally calculated value and with our previous calculation [38]. The magnetic moment of 0.681 μ_B is observed in the Cu atoms which is in good agreement with the experimental reported value of 0.69 μ_B [84].

The partial density of states (PDOS) for the pure and Ce doped CuO is presented in Fig. 11 with different Ce concentrations. The valance band region is formed by strongly hybridized Cu 3d and O 2p states where the contribution of O 2p states are higher than Cu 3d states. On the other

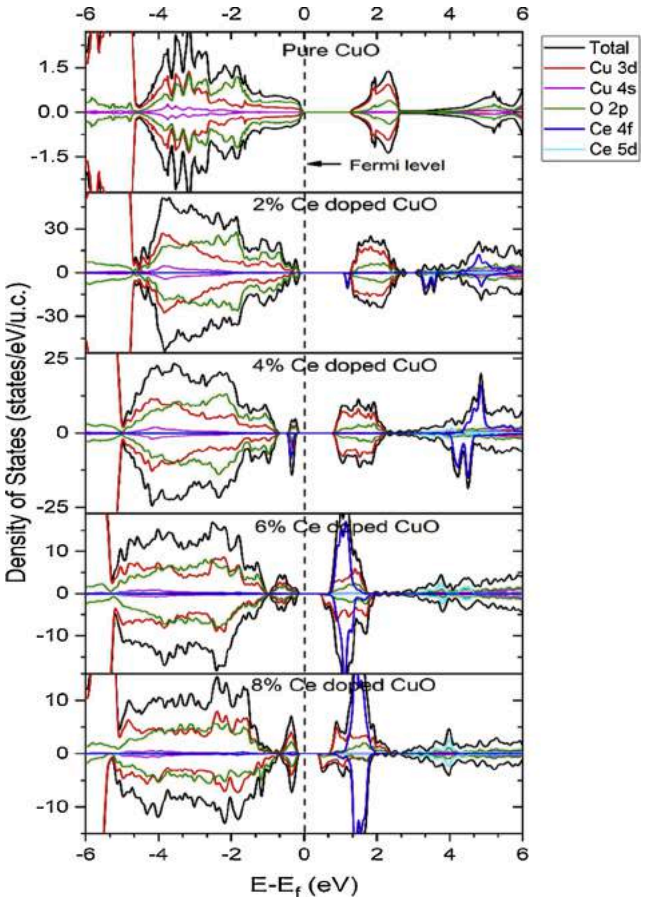

Fig. 11. Projected density of states of pure CuO and Ce doped CuO.

hand, the conduction band region also has a contribution from Cu 3d and O 2p states but the contribution of Cu 3d states are higher in the lower conduction band region (from 1.65 eV to 2.33 eV) but very low contribution in the higher conduction band region (from 2.4 eV to 5.8 eV). So, the O 2p states and the Cu 3d states are mainly responsible for the valence band and conduction band regions respectively. Hybridizing these states with impurity states can affect the bandgap and other electronic properties.

In the Ce doped cases, the contribution from Ce 4f states is more significant than Ce 5d (see Fig. 11). The Ce 4f states significantly affect the valence band and conduction band region and introduce defect states near the valence and conduction band region in the case of 2% Ce doped CuO system. These defect states are shallow states which are closely attached to the valence and conduction band. These shallow defect states can act as trap states for the charge carriers. Electrons can get trapped in the shallow defect states close to the valence band, and the hole can get trapped in the states close to the conduction band. The carrier's recombination process is inhibited by these shallow trap states. Due to the lower recombination process i.e. better quantum efficiency, degradation percentage increases for 2% doped case which is around 99 % found in our experiment after 30 min of irradiation compared to 60 % for the pure CuO.

Table 2
Bandgap of pure CuO and Ce doped CuO with a different configuration.

System	Bandgap (eV)
Pure CuO	1.74
2% Ce-doped	1.35
4% Ce-doped	1.40
6% Ce-doped	1.65
8% Ce-doped	1.63

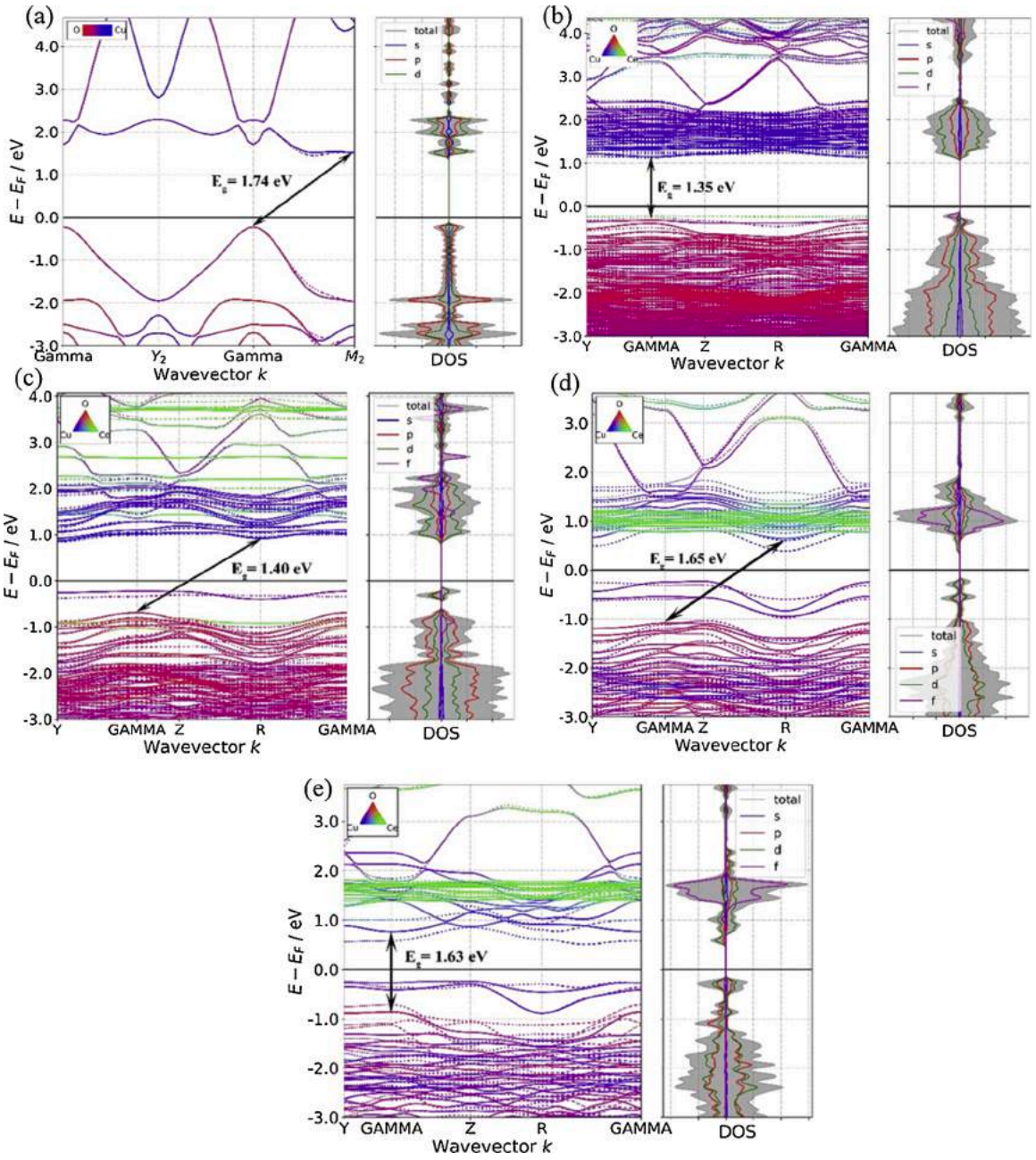

Fig. 12. Band structure of (a) pure, (b) 2%, (c) 4%, (d) 6%, and (e) 8% Ce doped CuO.

As the doping concentration increases, deep impurity states are formed very close to the Fermi level. In the 4% Ce doped case the defect states seem to be completely localized and close to the Fermi level. These deep states can act as a recombination center and decrease the degradation percentage. The same goes for 6% and 8% cases. This is one of the reasons we get a better degradation result for 2% Ce doped CuO only.

We have also calculated the band structure for pure and Ce doped CuO (see Fig. 12). The corresponding bandgaps are given in Table 2. The number of bands is increasing in the supercell, with the increasing number of atoms. CuO is an anti-ferromagnetic material. To measure the bandgap, we have considered the spin majority carrier i.e. spin-up electrons.

Pure CuO has an indirect bandgap (1.74 eV). But interestingly for 2% Ce doped case, it shows a direct bandgap of 1.35 eV. Which is close to our experimentally found optical band gap (1.4 eV). The rest of the doped systems show indirect bandgap except an 8% case. Only 2% Ce doped CuO system shows the lowest bandgap while for the other concentration bandgap increases gradually. The low band gap of of 1.35 eV may enhance the risk of carrier recombination. However, the Ce- doping introduce defect states near the valence and conduction band region. These shallow defect states can act as trap states for the charge carriers thereby reduce the charge carrier recombination rate and foster the photocatalytic efficiency [85,86].

3.7.2. *Optical properties*

We have calculated the real part of the dielectric, the imaginary part of the dielectric, and the absorption coefficient for the pure and Ce doped CuO system. The absorption coefficient is shown in Fig. 13(a). Due to the narrow bandgap, pure CuO can absorb UV light as well as visible light. Solar absorption increases near-visible range after Ce doping, due to some significant changes in the structure, introduction of impurity states, and change in the composition of energy bands.

Around the visible light range absorption coefficient increases as the doping concentration increases. Defect states near the valence band and deep impurity states played an important role here. As the concentration of Ce is increasing the density of states at the top of the valence band is also increasing resulting in a higher occupation possibility of electrons on the top of the valence band [87]. Moreover, for 4%–8% Ce concentrations, the density of states of the localized deep states increases noticeably. These impurity deep states are below the Fermi level so that they can be occupied by electrons. Thus, low energy photons can excite the electrons into the conduction band which in turn increases the absorption. The same trend is found in the imaginary part of the dielectric function near 2 eV (see Fig. 13(b,c)).

The real part of the dielectric is closely related to the recombination rate. Higher the real part of the dielectric lowers the recombination rate. Around 2 eV (almost the middle point of the visible light spectrum) real part of the dielectric for 2% is the highest (see Fig. 13 b) which is a clear indication for a better degradation rate.

4. Conclusions

In summary, CuO and Ce-doped CuO NPs were successfully synthesized by a cost-effective, simple sol-gel auto-combustion process. The XRD investigation revealed the presence of the monoclinic CuO nanoparticle and reduction in crystallite size due to Ce doping. The surface morphology of the NPs also reveals a reduction in particle size due to Ce doping. Raman spectroscopy of the Ce:CuO nanoparticle shows the presence of intrinsic defects due to Ce doping. Band gap of CuO NPs was found to be reduced from 1.72 eV to 1.40 eV for 2% Ce doping. Excessive doping of Ce greater than 2% enhances the band gap further. The visible light photocatalysis studies showed that Ce doping improves the photocatalytic activity of CuO NPs. The higher surface area of the NPs due to smaller particle size distribution together with its lower band gap is responsible for the enhanced photocatalytic activity of Ce:CuO. Density Functional Theory (DFT) simulations demonstrate that the incorporation of Ce on the CuO reduces the band gap of the NPs. It was also found that the Ce-dopant introduced shallow trap states near the valance band maxima and conduction band minima. Therefore, the reduced band gap together with the presence of these shallow trap states will in turn contribute to the efficient charge separation and enhanced light adsorption for Ce doped CuO NPS, resulting in improved photocatalytic activity. Finally, it can be concluded that the Ce doped CuO NPs synthesized by an effective and economic method may provide a sustainable approach to enhance the photocatalytic activity of CuO NPs and can found their applications in water purification and environment cleaning.

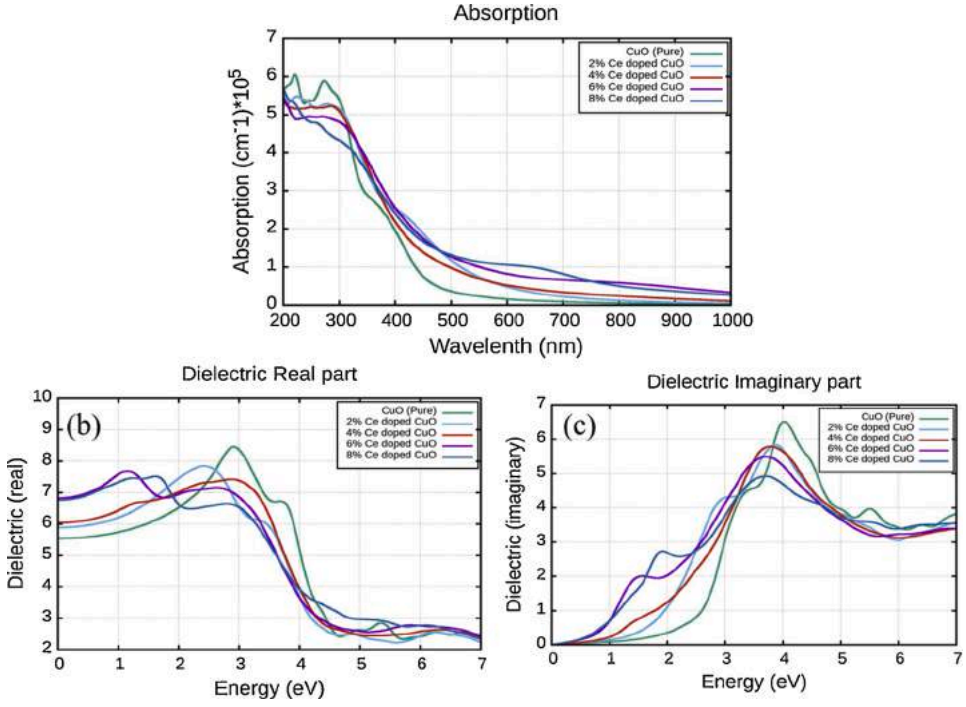

Fig. 13. The absorption (a), imaginary part of dielctric function (b), and (c) the real part of the dielectric function.

CRediT authorship contribution statement

Muhammad Rakibul Islam: Conceptualization, Methodology, Writing - original draft, Supervision. **Md. Saiduzzaman:** Formal analysis, Investigation. **Sadiq Shahriyar Nishat:** Software, Validation. **Alamgir Kabir:** Conceptualization, Writing - review & editing. **S.F.U. Farhad:** Investigation.

Declaration of Competing Interest

The authors report no declarations of interest.

Acknowledgement

Section: S.F.U. Farhad acknowledges the experimental supports under the scope of project #100-FY2017-2020.

References

[1] A. Mills, R.H. Davies, D. Worsley, Water purification by semiconductor photocatalysis, Chem. Soc. Rev. 22 (1993) 417–425.
[2] J. Gröttrup, et al., Porous ceramics based on hybrid inorganic tetrapodal networks for efficient photocatalysis and water purification, Ceram. Int. 43 (2017) 14915–14922.
[3] P.V. Kamat, D. Meisel, Nanoparticles in advanced oxidation processes, Curr. Opin. Colloid Interface Sci. 7 (2002) 282–287.
[4] A. Fujishima, X. Zhang, D.A. Tryk, TiO2 photocatalysis and related surface phenomena, Surf. Sci. Rep. 63 (2008) 515–582.
[5] R. Fagan, D.E. McCormack, D.D. Dionysiou, S.C. Pillai, A review of solar and visible light active TiO2 photocatalysis for treating bacteria, cyanotoxins and contaminants of emerging concern, Mater. Sci. Semicond. Process. 42 (2016) 2–14.
[6] K.M. Lee, C.W. Lai, K.S. Ngai, J.C. Juan, Recent developments of zinc oxide based photocatalyst in water treatment technology: a review, Water Res. 88 (2016) 428–448.
[7] K. Qi, B. Cheng, J. Yu, W. Ho, Review on the improvement of the photocatalytic and antibacterial activities of ZnO, J. Alloys. Compd. 727 (2017) 792–820.
[8] C.R. Rajith Kumar, et al., One-pot green synthesis of ZnO-CuO nanocomposite and their enhanced photocatalytic and antibacterial activity, Adv. Nat. Sci. Nanosci. Nanotechnol. 11 (2020).
[9] M. Ahmadian, M. Anbia, M. Rezaie, Sulfur dioxide removal from flue gas by supported CuO nanoparticle adsorbents, Ind. Eng. Chem. Res. 59 (2020) 21642–21653.
[10] K.R. Park, et al., Design of highly porous SnO2-CuO nanotubes for enhancing H2S gas sensor performance, Sensors Actuators, B Chem. 302 (2020).
[11] R. Molavi, M.H. Sheikhi, Facile wet chemical synthesis of Al doped CuO nanoleaves for carbon monoxide gas sensor applications, Mater. Sci. Semicond. Process. 106 (2020).
[12] G.K. Weldegebrieal, Photocatalytic and antibacterial activityof CuO nanoparticles biosynthesized using Verbascum thapsus leaves extract, Optik (Stuttg). 204 (2020).
[13] S.F.U. Farhad, D. Cherns, J.A. Smith, N.A. Fox, D.J. Fermín, Pulsed laser deposition of single phase n- and p-type Cu2O thin films with low resistivity, Mater. Des. 193 (2020).
[14] S.F.U. Farhad, R.F. Webster, D. Cherns, Electron microscopy and diffraction studies of pulsed laser deposited cuprous oxide thin films grown at low substrate temperatures, Materialia 3 (2018) 230–238.
[15] S. Varnagiris, et al., Floating TiO2 photocatalyst for efficient inactivation of E. Coli and decomposition of methylene blue solution, Sci. Total Environ. 720 (2020).
[16] R. Gusain, P. Kumar, O.P. Sharma, S.L. Jain, O.P. Khatri, Reduced graphene oxide-CuO nanocomposites for photocatalytic conversion of CO2 into methanol under visible light irradiation, Appl. Catal. B Environ. 181 (2016) 352–362.
[17] M.P. Rao, J.J. Wu, A.M. Asiri, S. Anandan, M. Ashokkumar, Photocatalytic properties of hierarchical CuO nanosheets synthesized by a solution phase method, J. Environ. Sci. (China) 69 (2018) 115–124.
[18] S. Sonia, et al., Hydrothermal synthesis of novel Zn doped CuO nanoflowers as an efficient photodegradation material for textile dyes, Mater. Lett. 144 (2015) 127–130.
[19] S.P. Meshram, P.V. Adhyapak, U.P. Mulik, D.P. Amalnerkar, Facile synthesis of CuO nanomorphs and their morphology dependent sunlight driven photocatalytic properties, Chem. Eng. J. 204–205 (2012) 158–168.
[20] B.M. Abu-Zied, S.M. Bawaked, S.A. Kosa, W. Schwieger, Effect of some rare earth oxides doping on the morphology, crystallite size, electrical conductivity and N2O decomposition activity of CuO catalyst, Int. J. Electrochem. Sci. 11 (2016) 1568–1580.
[21] L. Vimala Devi, et al., Synthesis, defect characterization and photocatalytic degradation efficiency of Tb doped CuO nanoparticles, Adv. Powder Technol. 28 (2017) 3026–3038.
[22] N. Ekthammathat, A. Phuruangrat, T. Thongtem, S. Thongtem, Synthesis and characterization of Ce-doped CuO nanostructures and their photocatalytic activities, Mater. Lett. 167 (2016) 266–269.
[23] M. Iqbal, et al., Influence of Mn-doping on the photocatalytic and solar cell efficiency of CuO nanowires, Inorg. Chem. Commun. 76 (2017) 71–76.
[24] A. Pugazhendhi, S.S. Kumar, M. Manikandan, M. Saravanan, Photocatalytic properties and antimicrobial efficacy of Fe doped CuO nanoparticles against the pathogenic bacteria and fungi, Microb. Pathog. 122 (2018) 84–89.
[25] Y. Chen, et al., Effect of doping Ce ions on morphology and photocatalytic activity of CuO nanostructures, Cryst. Res. Technol. 54 (2019).
[26] S.P. Chaudhari, A.B. Bodade, P.D. Jolhe, S.P. Meshram, G.N. Chaudhari, PEG-200 assisted sonochemical synthesis of cerium (Ce 3+) doped copper oxide (CuO) nanocomposites and their photocatalytic activities, Am. J. Mater. Synth. Process. 2 (2017) 97–102.
[27] M. Xing, et al., Modulating Cu+ distribution on the surface of Ce-doped CuO composite oxides for SO2-resistant NH3-selective catalytic reduction of NO, RSC Adv. 7 (2017) 18830–18837.
[28] M. Ponnar, C. Thangamani, P. Monisha, S.S. Gomathi, K. Pushpanathan, Influence of Ce doping on CuO nanoparticles synthesized by microwave irradiation method, Appl. Surf. Sci. 449 (2018) 132–143.
[29] P. Chen, et al., Rare-earth single-atom La-N charge-transfer bridge on carbon nitride for highly efficient and selective photocatalytic CO2 reduction, ACS Nano 14 (2020) 15841–15852.
[30] F. Dong, et al., Identification of halogen-associated active sites on bismuth-based perovskite quantum dots for efficient and selective CO2-to-CO photoreduction, ACS Nano 14 (2020) 13103–13114.
[31] J. Li, et al., Synergistic photocatalytic decomposition of a volatile organic compound mixture: high efficiency, reaction mechanism, and long-term stability, ACS Catal. 10 (2020) 7230–7239.
[32] Z.N. Kayani, M. Umer, S. Riaz, S. Naseem, Characterization of copper oxide nanoparticles fabricated by the sol–Gel method, J. Korean Inst. Electr. Electron. Mater. Eng. 44 (2015) 3704–3709.
[33] C.C. Vidyasagar, Y.A. Naik, T.G. Venkatesh, R. Viswanatha, Solid-state synthesis and effect of temperature on optical properties of Cu-ZnO, Cu-CdO and CuO nanoparticles, Powder Technol. 214 (2011) 337–343.
[34] X. Zhang, D. Zhang, X. Ni, H. Zheng, Optical and electrochemical properties of nanosized CuO via thermal decomposition of copper oxalate, Solid. Electron. 52 (2008) 245–248.
[35] A. Sutka, G. Mezinskis, Sol-gel auto-combustion synthesis of spinel-type ferrite nanomaterials, Front. Mater. Sci. 6 (2012) 128–141.
[36] I. Singh, R.K. Bedi, Surfactant-assisted synthesis, characterizations, and room temperature ammonia sensing mechanism of nanocrystalline CuO, Solid State Sci. 13 (2011) 2011–2018.
[37] M.R. Islam, M. Rahman, S.F.U. Farhad, J. Podder, Structural, optical and photocatalysis properties of sol–gel deposited Al-doped ZnO thin films, Surf. Interfaces 16 (2019) 120–126.
[38] M.R. Islam, et al., Effect of Al doping on the structural and optical properties of CuO nanoparticles prepared by solution combustion method: experiment and DFT investigation, J. Phys. Chem. Solids 147 (2020), 109646.
[39] G. Kresse, J. Furhmuller, Software VASP, Vienna (1999); Kresse G. And hafner, Phys. Rev. B 47 (R558) (1993).
[40] J. Paier, R. Hirschl, M. Marsman, G. Kresse, The Perdew-Burke-Ernzerhof exchange-correlation functional applied to the G2-1 test set using a plane-wave basis set, J. Chem. Phys. 122 (2005).
[41] V.I. Anisimov, J. Zaanen, O.K. Andersen, Band theory and Mott insulators: hubbard U instead of Stoner I, Phys. Rev. B 44 (1991) 943–954.
[42] H. Hsu, P. Blaha, R.M. Wentzcovitch, C. Leighton, Cobalt spin states and hyperfine interactions in LaCoO3 investigated by LDA+U calculations, Phys. Rev. B - Condens. Matter Mater. Phys. 82 (2010).
[43] H. Hsu, K. Umemoto, M. Cococcioni, R. Wentzcovitch, First-principles study for low-spin LaCoO3 with a structurally consistent Hubbard U, Phys. Rev. B - Condens. Matter Mater. Phys. 79 (2009).
[44] A.V. Krukau, O.A. Vydrov, A.F. Izmaylov, G.E. Scuseria, Influence of the exchange screening parameter on the performance of screened hybrid functionals, J. Chem. Phys. 125 (2006).
[45] F. Aryasetiawan, O. Gunnarsson, The GW method, Rep. Prog. Phys. 61 (1998) 237–312.
[46] M. Heinemann, B. Eifert, C. Heiliger, Band structure and phase stability of the copper oxides Cu2O, CuO, and Cu4O3, Phys. Rev. B - Condens. Matter Mater. Phys. 87 (2013).
[47] L. Honglin, L. Yingbo, L. Jinzhu, Y. Ke, Experimental and first-principles studies of structural and optical properties of rare earth (RE = La, Er, Nd) doped ZnO, J. Alloys. Compd. 617 (2014) 102–107.
[48] X. Ma, Y. Wu, Y. Lv, Y. Zhu, Correlation effects on lattice relaxation and electronic structure of zno within the GGA+ U formalism, J. Phys. Chem. C 117 (2013) 26029–26039.
[49] J.P. Perdew, K. Burke, M. Ernzerhof, Generalized gradient approximation made simple, Phys. Rev. Lett. 77 (1996) 3865–3868.
[50] H.J. Monkhorst, J.D. Pack, Special points for Brillouin-zone integrations, Phys. Rev. B 13 (1976) 5188–5192.
[51] Y. Maimaiti, M. Nolan, S.D. Elliott, Reduction mechanisms of the CuO(111) surface through surface oxygen vacancy formation and hydrogen adsorption, Phys. Chem. Chem. Phys. 16 (2014) 3036–3046.
[52] C.E. Ekuma, V.I. Anisimov, J. Moreno, M. Jarrell, Electronic structure and spectra of CuO, Eur. Phys. J. B 87 (2014) 1–6.
[53] M. Nolan, S.D. Elliott, The p-type conduction mechanism in Cu2O: a first principles study, Phys. Chem. Chem. Phys. 8 (2006) 5350–5358.

[54] S. Fabris, G. Vicario, G. Balducci, S. De Gironcoli, S. Baroni, Electronic and atomistic structures of clean and reduced ceria surfaces, J. Phys. Chem. B 109 (2005) 22860–22867.
[55] M. Capdevila-Cortada, Z. Łodziana, N. López, Performance of DFT+U approaches in the study of catalytic materials, ACS Catal. 6 (2016) 8370–8379.
[56] P. Deniard, et al., High potential positive materials for lithium-ion batteries: transition metal phosphates, J. Phys. Chem. Solids 65 (2004) 229–233.
[57] T. Jiang, et al., Controllable fabrication of CuO nanostructure by hydrothermal method and its properties, Appl. Surf. Sci. 311 (2014) 602–608.
[58] J. Bai, Z. Xu, Y. Zheng, H. Yin, Shape control of CeO2 nanostructure materials in microemulsion systems, Mater. Lett. 60 (2006) 1287–1290.
[59] M. Faisal, A.A. Ismail, A.A. Ibrahim, H. Bouzid, S.A. Al-Sayari, Highly efficient photocatalyst based on Ce doped ZnO nanorods: controllable synthesis and enhanced photocatalytic activity, Chem. Eng. J. 229 (2013) 225–233.
[60] M. Faisal, A.A. Ismail, A.A. Ibrahim, H. Bouzid, S.A. Al-Sayari, Highly efficient photocatalyst based on Ce doped ZnO nanorods: controllable synthesis and enhanced photocatalytic activity, Chem. Eng. J. 229 (2013) 225–233.
[61] R. Kumar, et al., Ce-doped ZnO nanoparticles for efficient photocatalytic degradation of direct red-23 dye, Ceram. Int. 41 (2015) 7773–7782.
[62] S. Liu, et al., Fabrication of p-type ZnO nanofibers by electrospinning for field-effect and rectifying devices, Appl. Phys. Lett. 104 (2014).
[63] R.I. Chowdhury, et al., Characterization of chemically deposited cadmium sulfide thin films, Int. J. Mod. Phys. B 24 (2010) 5901–5911.
[64] Y.J. Liu, et al., Effect of Ce doping on the optoelectronic and sensing properties of electrospun ZnO nanofibers, RSC Adv. 6 (2016) 85727–85734.
[65] T. Yu, X. Zhao, Z.X. Shen, Y.H. Wu, W.H. Su, Investigation of individual CuO nanorods by polarized micro-Raman scattering, J. Cryst. Growth 268 (2004) 590–595.
[66] I. Kosacki, T. Suzuki, H.U. Anderson, P. Colomban, Raman scattering and lattice defects in nanocrystalline CeO2 thin films, Solid State Ion. 149 (2002) 99–105.
[67] V. Lughi, D.R. Clarke, Defect and stress characterization of AlN films by Raman spectroscopy, Appl. Phys. Lett. 89 (2006).
[68] K. Mageshwari, R. Sathyamoorthy, Organic free synthesis of flower-like hierarchical CuO microspheres by reflux condensation approach, Appl. Nanosci. 3 (2013) 161–166.
[69] C. Yang, et al., Facile microwave-assisted hydrothermal synthesis of varied-shaped CuO nanoparticles and their gas sensing properties, Sensors Actuators, B Chem. 185 (2013) 159–165.
[70] M. Lenglet, et al., Low temperature oxidation of copper: the formation of CuO, Mater. Res. Bull. 30 (1995) 393–403.
[71] H.W. Wu, S.Y. Lee, W.C. Lu, K.S. Chang, Piezoresistive effects enhanced the photocatalytic properties of Cu 2 O/CuO nanorods, Appl. Surf. Sci. 344 (2015) 236–241.
[72] G. Borghs, K. Bhattacharyya, K. Deneffe, P. Van Mieghem, R. Mertens, Band-gap narrowing in highly doped n- and p-type GaAs studied by photoluminescence spectroscopy, J. Appl. Phys. 66 (1989) 4381–4386.
[73] T. Jan, et al., Synthesis, physical properties and antibacterial activity of Ce doped CuO: a novel nanomaterial, J. Phys. D Appl. Phys. 47 (2014).
[74] S. Rajendran, et al., Ce3+-ion-induced visible-light photocatalytic degradation and electrochemical activity of ZnO/CeO2 nanocomposite, Sci. Rep. 6 (2016).
[75] Y.H. Yang, X.Y. Chen, Y. Feng, G.W. Yang, Physical mechanism of blue-shift of UV luminescence of a single pencil-like ZnO nanowire, Nano Lett. 7 (2007) 3879–3883.
[76] B. Tiss, M. Erouel, N. Bouguila, M. Kraini, K. Khirouni, Effect of silver doping on structural and optical properties of In2S3 thin films fabricated by chemical pyrolysis, J. Alloys. Compd. 771 (2019) 60–66.
[77] M.I. Litter, J.A. Navío, Photocatalytic properties of iron-doped titania semiconductors, J. Photochem. Photobiol. A: Chem. 98 (1996) 171–181.
[78] Y. Liang, et al., Preparation of porous 3D Ce-doped ZnO microflowers with enhanced photocatalytic performance, RSC Adv. 5 (2015) 59887–59894.
[79] X.H. Wang, J.G. Li, H. Kamiyama, Y. Moriyoshi, T. Ishigaki, Wavelength-sensitive photocatalytic degradation of methyl orange in aqueous suspension over iron(III)-doped TiO2 nanopowders under UV and visible light irradiation, J. Phys. Chem. B 110 (2006) 6804–6809.
[80] L. Wang, Z. Ji, J. Lin, P. Li, Preparation and optical and photocatalytic properties of Ce-doped ZnO microstructures by simple solution method, Mater. Sci. Semicond. Process. 71 (2017) 401–408.
[81] R. Mohan, K. Krishnamoorthy, S.J. Kim, Enhanced photocatalytic activity of Cu-doped ZnO nanorods, Solid State Commun. 152 (2012) 375–380.
[82] S. Singh, R. Sharma, B.R. Mehta, Enhanced surface area, high Zn interstitial defects and band gap reduction in N-doped ZnO nanosheets coupled with BiVO 4 leads to improved photocatalytic performance, Appl. Surf. Sci. 411 (2017) 321–330.
[83] R. Sharma, M. Khanuja, S.N. Sharma, O.P. Sinha, Reduced band gap & charge recombination rate in Se doped A-Bi2O3 leads to enhanced photoelectrochemical and photocatalytic performance: theoretical & experimental insight, Int. J. Hydrogen Energy 42 (2017) 20638–20648.
[84] B.X. Yang, T.R. Thurston, J.M. Tranquada, G. Shirane, Magnetic neutron scattering study of single-crystal cupric oxide, Phys. Rev. B 39 (1989) 4343–4349.
[85] W. Zhou, H. Fu, Defect-mediated electron-hole separation in semiconductor photocatalysis, Inorg. Chem. Front. 5 (2018) 1240–1254.
[86] D. Ramírez-Ortega, D. Guerrero-Araque, P. Acevedo-Peña, L. Lartundo-Rojas, R. Zanella, Effect of Pd and Cu co-catalyst on the charge carrier trapping, recombination and transfer during photocatalytic hydrogen evolution over WO3–TiO2 heterojunction, J. Mater. Sci. 55 (2020) 16641–16658.
[87] Q.L. Liu, Z.Y. Zhao, Q.J. Liu, Analysis of sulfur modification mechanism for anatase and rutile TiO 2 by different doping modes based on GGA + U calculations, RSC Adv. 4 (2014) 32100–32107.